8

Beam halo horizontal distribution measurements at ATF2

After characterising the "in vacuum" diamond sensor (DSv) at ATF2, beam core and halo transverse horizontal distribution was measured at ATF2 in Nov.-Dec. 2014. Beam core measurements were used for the normalisation of the beam halo distribution. In this chapter, the data taking and analysis procedures are described. Beam core and beam halo distributions measured with different beam intensities and beam optics are presented and compared.

8.1 Data taking procedures

The data taking procedures defined for the measurements are shown as below:

- DSv horizontal centering: beam core scan using DSv with low bias voltage (-40 V) to find the horizontal beam center;
- Vertical Alignment (VA): move the AQD0FF mover to steer the beam vertically and find the vertical beam center, where the signal on the DSv is maximum;
- Post-IP wire scanner beam core scan: scan the beam core use the Post-IP wire scanner to get the horizontal and vertical beam size for beam size verification;
- DSv beam core scan: beam core scan using the DSv after VA with high bias voltage (-400 V) and 30 dB attenuators;

- Beam core fitting: fit the beam core to get the beam size and define the beam halo scan region;
- DSv beam halo scan: beam halo scan using the DSv with a bias voltage of -400 V without attenuators in the region of $<$-3σ for the low energy side (left side) and $>$3σ for the high energy side (right side).

8.2 Data analysis procedures

The data analysis procedures consist of pedestal subtraction, ICT correction and data binning, which are explained in more detail in the following subsections.

8.2.1 Pedestal subtraction

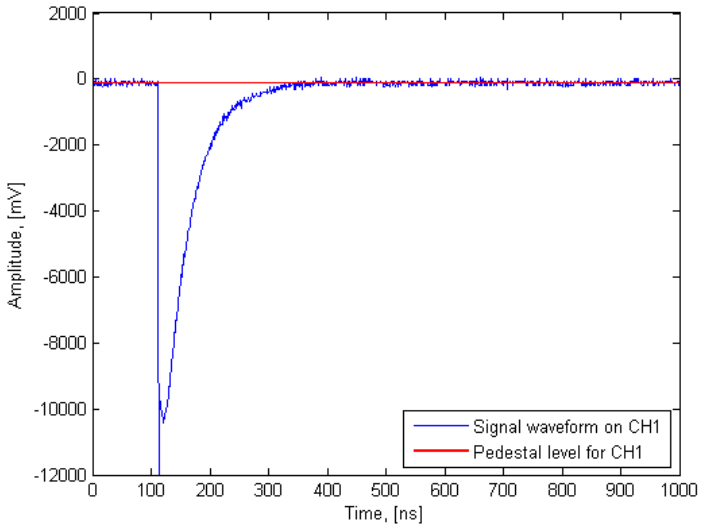

Figure 8.1: Pedestal definition

Signal waveforms have a certain level of pedestal as the Agilent oscilloscope is not well calibrated. The pedestal level of each channel is different and it changes with the vertical range (VR) setting. Therefore, pedestal subtraction is quite essential for the data analysis.

The pedestal level is defined for each waveforms by taking average value of the points before the arrival of signal (see Fig.8.1). In order to get a better statistics for

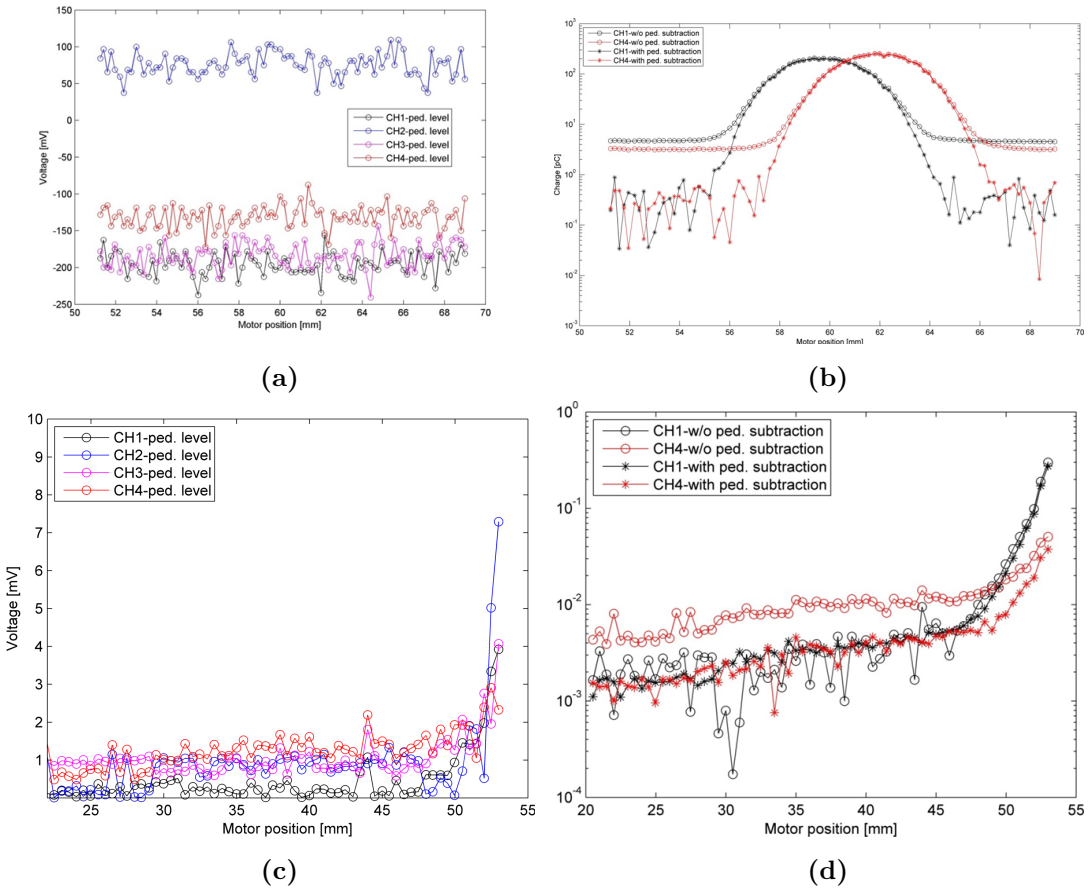

Figure 8.2: Pedestal level measured during the scan of the beam core (a) and beam halo (c); Beam core (b) and beam halo (d) distribution before and after pedestal subtraction.

the pedestal calculation, in the experiment a delay of 1 division of full timebase (1/10 of full timebase) was set to ensure at least 100 points for averaging. Then the pedestal level is again averaged over 10 waveforms. After that, the averaged pedestal level is subtracted for each waveform.

Fig. 8.2 shows the measured average pedestal level during the scan and the beam core and beam halo distribution before and after pedestal subtraction. It can be seen from Fig. 8.2 (a) that for the beam core scan, as the scope VR is a constant, the pedestal level is also stable during the scan. However, for the beam halo scan (Fig. 8.2 (c)), as the scope VR changes at each point, the pedestal level is also changed. Depending on the signal level, the pedestal level can range from several mV for beam halo to ∼100 mV for beam core. From Fig.8.2 (d) it can be seen that for the beam

halo distribution, after pedestal subtraction the integrated signal charge from CH1 is more consistent with signal from CH4 than before pedestal subtraction.

8.2.2 ICT correction

The ICT data obtained through the EPICS system as mentioned in 7.4.1 provides the information of the total number of electrons (N_t) in the beam. As N_t may fluctuate from pulse to pulse, ICT correction was done to check the effect of ICT fluctuation on the beam halo distribution.

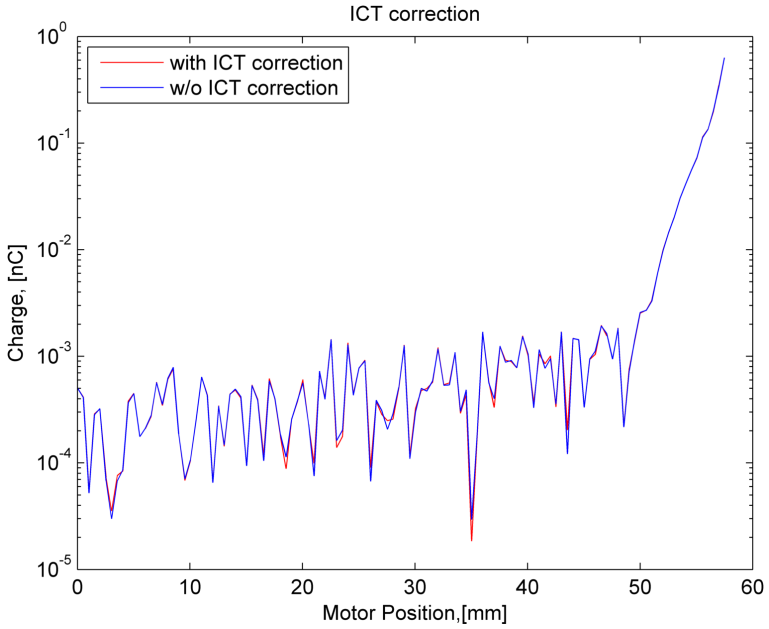

Figure 8.3: Beam halo distribution with (red) and without (blue) ICT correction

For the ICT correction, first the mean ICT value (ICT_{mean}) was calculated from all the ICT values registered during the whole scan. As 10 waveforms were taken at each point, then the ICT_{mean} can be expressed as:

$$ICT_{mean} = \frac{\sum_{i=1}^{i=10\times N_{points}} ICT_i}{10 \times N_{points}} \tag{8.1}$$

Then the integrated charge for each waveform (Q_i) can be corrected as:

$$Q_{i_{correct}} = Q_i \times \frac{ICT_i}{ICT_{mean}} \tag{8.2}$$

Fig.8.3 shows the averaged integrated charge along the scan positions before (in blue) and after (in red) ICT correction. The calculated ICT_{mean} value here is 4.466×10^9 e^- while the standard deviation of ICT is 0.442×10^9 e^-. It can be seen that the effect of ICT correction on the integrated charge is negligible.

Meanwhile, the beam jitter during the scan is estimated to be around 45.60 μm on X and 31.97 μm on Y at the post-IP BPM location, which is also very small compare with the strip width of 1.5 mm. Therefore we assume that the fluctuation on the charge distribution is due to the signal pick-up as presented in Section 7.5.1. Since the auto scope vertical range setting system (see section 7.4.3 and 7.5.1) takes the signal amplitude as a criteria to define the VR, and the charge is integrated for the whole waveform, a relatively high amplitude of signal pick-up caused a relatively high VR, consequently, a bad resolution.

8.2.3 Data binning

In order to reduce the fluctuations in the distribution, the data were re-binned. The number of bins is chosen in order to ensure at least 1 data point per bin. The value of each bin correspond to the mean value of the points in this bin. Fig.8.4 shows an example of data taken for different optics without (a) and with (b) binning the data. It can be seen that data binning has improved the visibility of the distribution.

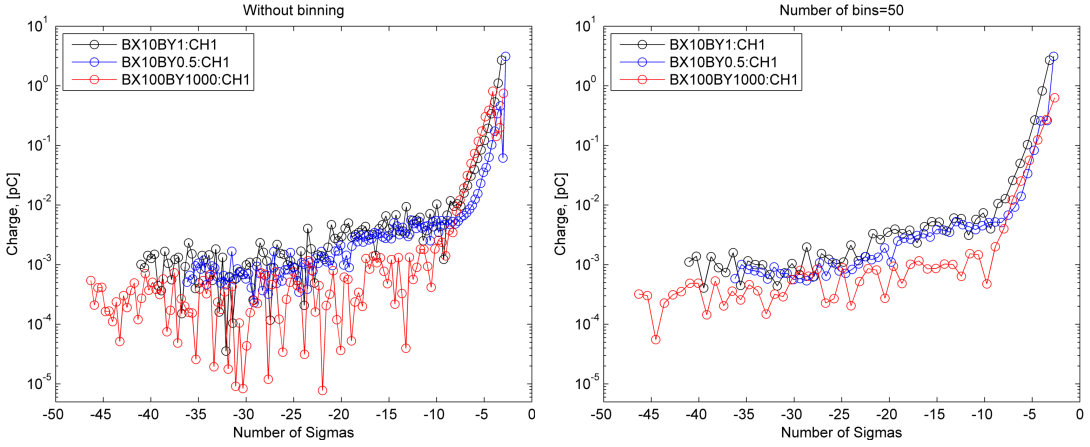

Figure 8.4: Beam halo distribution without (a) and with (b) binning

8.3 Beam core measurements

8.3.1 Vertical alignment

Before measuring the horizontal beam halo distribution, we have to make sure that the beam is vertically centered. Therefore, vertical alignment (VA) is required. For the VA at the DSv location, we first do a horizontal scan to find the horizontal beam center and keep the DSv in the horizontal center, and then move the beam vertically at the IP by changing the AQD0FF vertical mover position (AQD0FF mover position scan). The mover position can be changed max. by ± 1500 μm vertically and ± 2000 μm horizontally. The nominal vertical value of the mover is at 160 μm. During the alignment we move the mover by 50 μm/step from 100 μm to 900 μm and take 100 waveforms at each mover position and the integrated charge is plotted as a function of the vertical position of QD0, i.e. AQD0FF, as shown in Fig.8.5. From the plot we can find the position where the DSv collects the maximum charge (minimum value in the plot, since the bias voltage applied to the DSv is negative), which means that the beam is vertically centered.

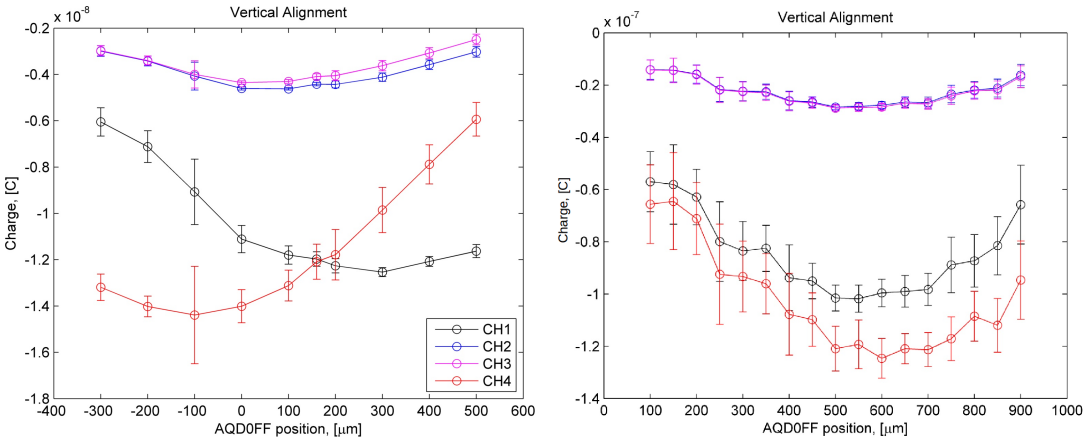

(a) **(b)**

Figure 8.5: Vertical alignment of beam by moving the AQD0FF mover vertically: (a) tilted beam (data taken on 18-12-2015 at -400 V with 30 dB attenuator) ; (b) not tilted beam (data taken on 05-12-2015 at -40 V without attenuator)

If the beam is not tilted, the vertical center should be the same for both channels, which is the case shown in Fig.8.5 (b). However, if the beam is tilted in the transverse plane, then the vertical center can be different for different channels. This can be seen

from Fig.8.5 (a) where the valley of CH1 and CH4 are at different mover positions. In this case, it is difficult to define whether the beam is centered vertically or not and the measured beam halo distribution will not be correct. Therefore, for the beam halo measurement, it is important to make sure that the beam is not tilted by doing the AQD0FF mover position scan and correct the beam tilt if it exists.

The beam core scan before and after vertical alignment is shown in Fig.8.6. Obviously, after VA the collected charge is increased in all the channels. However, after VA we also found that the signal strength on CH4 is different from CH1, while there is almost no different between CH2 and CH3 (see Fig.8.7).

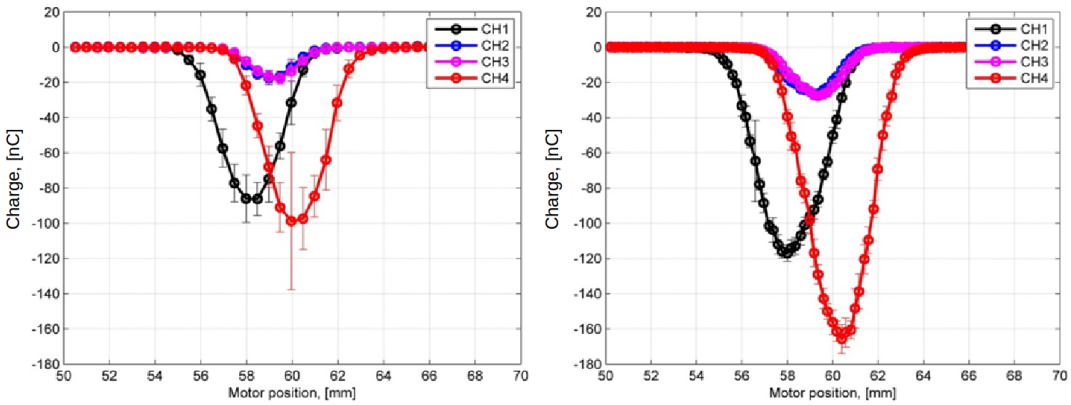

Figure 8.6: Beam core scan before (left) and after (right) vertical alignment (data taken on 05-12-2014 at -40 V without attenuator)

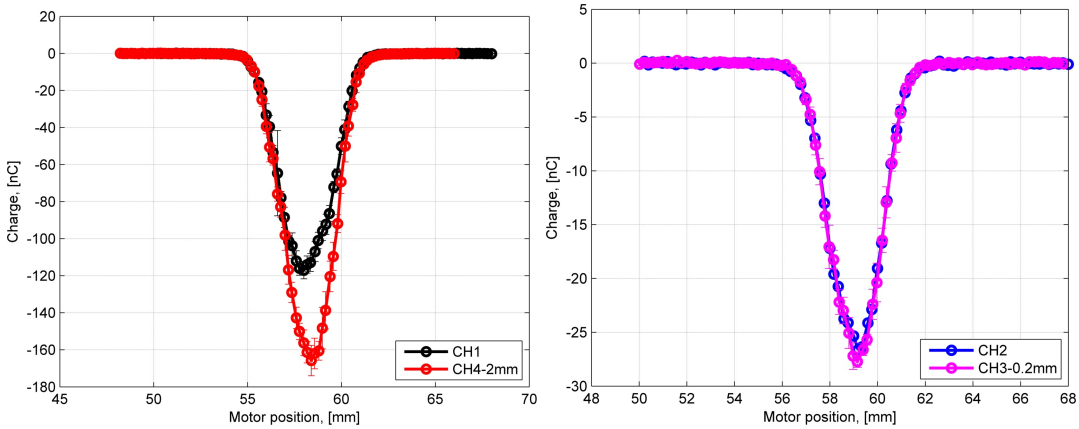

Figure 8.7: Beam core signal strength comparison between CH1 and CH4 (left) and between CH2 and CH3 (right) after vertical alignment, CH4 and CH3 are moved by 2 mm and 0.2 mm to match the position of CH1 and CH2, respectively.

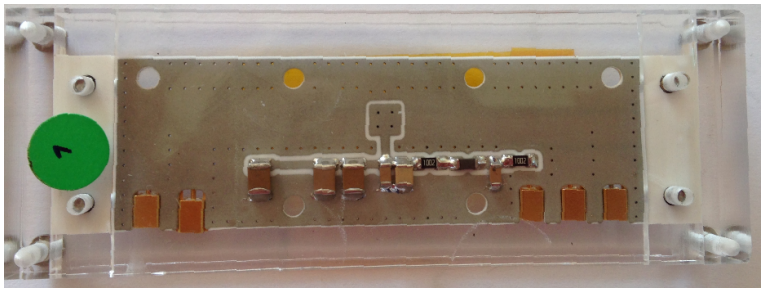

Figure 8.8: DSv bottom view

From Fig.8.7 it can be seen that the signal strength difference between CH1 and CH4 exist mainly in the region from 57 mm to 60 mm of motor position. This region correspond to the bias voltage supply line on the PCB and the region next to this is where the resistors and capacitors are situated. Therefore, we suspect that the difference in the signal strength on CH1 and CH4 in this region might be due to the beam core hitting the bias voltage supply line. This effect is not so strong when the beam is not centered vertically as shown in Fig. 8.6 (left), which means it can be verified by steering the beam vertically and compare the signal strength on CH1 and CH4. Further measurements need to be taken to verify this effect.

8.3.2 Beam core size verification

Comparison of beam core size measured by different channels

After the VA, beam core is scanned using DSv and the measured beam core signal is fitted using Eq. 7.8. An example of beam core fit is shown in Fig. 8.9. The fitted beam size (σ) by this Eq. 7.8 is corrected by the strip width (l). Each data point is weighted by a weight w=$1/\sigma^2$, and the fit weighted least-squares regression minimizes the error estimate S=$\sum_{i=1}^{n} w_i(y_i - \hat{y}_i)^2$, where y_i is the measured value, $\hat{y}_i$ is the fitted value. The error of the fitted parameters are obtained from the 95% confidence interval.

The beam sizes measured by different channels are compared in Table 8.1 for different beam optics. From the table it can be seen that CH1 and CH4 measures a larger beam size than CH2 and CH3. This is due to the saturation of collected charge in the beam core, which could be mitigated by applying appropriate calibrations. Thus, for the normalization of beam halo measurement, it is preferable to use the beam size measured by CH2 and CH3.

Comparing the beam size measured by CH1 and CH4, it can be seen that CH4 measures a smaller beam size than CH1. This is due to the previously mentioned effect that the signal strength on CH4 is higher than CH1. This effect get stronger when the vertical beam size (σ_y) get smaller [1]. As BX100BY1000 optics has the smallest σ_y comparing with the other two optics (see Table. 8.2), CH4 measured a smallest σ_y among all the channels.

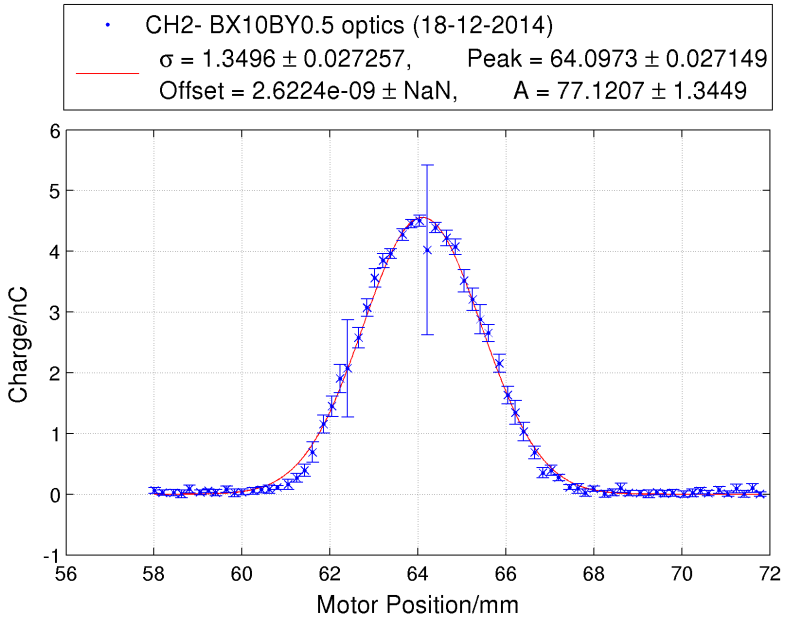

Figure 8.9: Example of beam core fit using Eq. 7.8 for CH2.

	BX10BY0.5(18-12-14)	BX10BY1(04-12-14)	BX100BY1000 (20-12-14)
CH1	1.401 $\pm$0.047mm	1.300 $\pm$0.046mm	1.261 $\pm$0.026mm
CH2	1.350 $\pm$0.027mm	1.362 $\pm$0.061mm	1.254 $\pm$0.025mm
CH3	1.261 $\pm$0.028mm	1.296 $\pm$0.063mm	1.208 $\pm$0.030mm
CH4	1.351 $\pm$0.023mm	1.272 $\pm$0.054mm	1.120 $\pm$0.031mm

Table 8.1: Comparison of measured beam size for different optics by different channels of DSv

[1]The simulated vertical beam size for BX100BY1000 optics is $\sim$0.04 mm, whereas for BX10BY1 and BX10BY0.5 are $\sim$1.3 mm (see Table 8.2).

Comparison between simulation and measurement

Table. 8.2 shows the comparison between simulated and measured beam size for post-IP wire scanner (post-IPW) and DSv. The simulated values are obtained from Mad-X simulation. The DSv expected values are calculated by multiplying the simulated value by the discrepancy factor obtained from post-IPW. It can be seen that the discrepancy between simulated and measured beam size is larger for post-IPW than for DSv. It could be that the DSv CH2 provides a more reliable beam size measurement than the post-IPW. This can be verified by further measurements using the vertical DSv scanner. If the discrepancy on the vertical plane is also smaller than the post-IPW, then DSv could serve as an instrument for beam size tuning in the future.

In the BX100BY1000 optics, as simulated σ_y is around 6.9 μm which is much smaller than the wire scanner thickness (50 μm), the post-IPW measured σ_y is not valid. Therefore, we couldn't calculate the expected σ_y for DSv.

For the calculation for number of intercepted electrons (N_{CH}) in section 7.5.4 in Equation 7.9, the DSv measured beam horizontal beam size by CH2 is used for σ_x, and the expected σ_y is used as vertical beam size except for the BX100BY1000 optics, where we used the simulated value. However, as the vertical width of DSv is 4 mm which is quite large compare to σ_y, the difference between using simulated or expected value is negligible.

	BX10BY0.5		BX10BY1		BX100BY1000	
	σ_x (mm)	σ_y (mm)	σ_x (mm)	σ_y (mm)	σ_x (mm)	σ_y (mm)
post-IPW simulated	0.156	0.289	0.156	0.216	8.744e-02	6.921e-03
post-IPW measured	0.197	0.571	0.266	0.429	6.150e-02 0	4.28e-02
DSv simulated	1.394	1.787	1.395	1.336	1.077	4.224e-02
DSv measured(CH2)	1.350±0.027	-	1.362±0.061	-	1.254±0.025	-
DSv expected	1.937	3.442	2.360	2.650	0.757	-

Table 8.2: Comparison of simulated and measured beam size at the post-IPW and the DSv position for different optics (The errors of post-IPW measured beam sizes are negligible.).

8.4 Beam halo measurements

8.4.1 Background from cables

After doing a complete beam halo scan, a "strange" peak on the high energy side of the beam was found at around $26\sigma_x$ from the beam center. This peak was caused by the beam core hitting the coaxial cables which were inserted into the vacuum chamber without proper fixing, because the distance between the cables and the beam center is ~40 mm, which correspond to $\sim 26\sigma_x$ as observed. The difficulty in fixing the cables is due to their rigidity. Besides, the PCB is very fragile and the connections to the MMCX connectors are very rigid. In order to settle this problem, the coaxial cables in the vacuum chamber were rearranged and fixed to the holder using more copper wires. Fig. 8.10 shows the photo and measurements taken before and after fixing the cables.

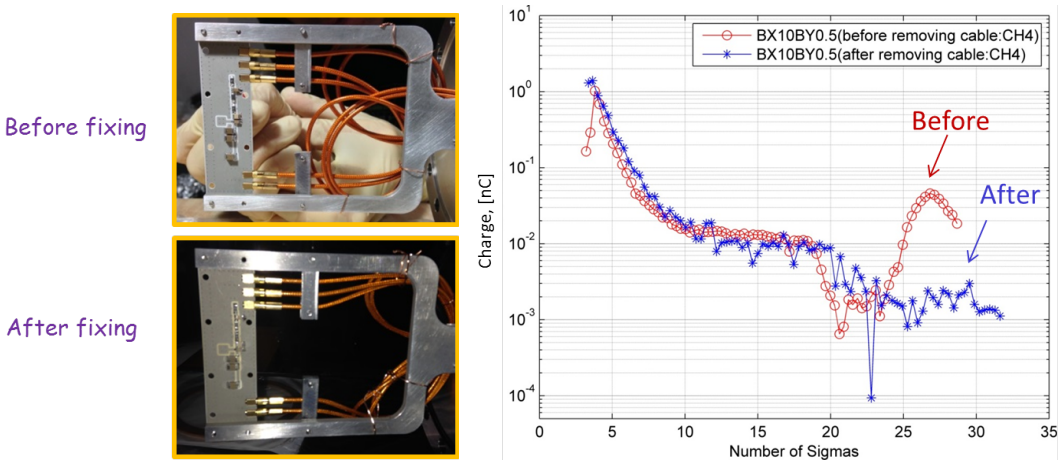

Figure 8.10: Left: photo taken before (upper) and after (lower) fixing the cable; Right: measured signal before and after fixing the cable.

It can be seen that after fixing the cable, the "strange" peak disappeared while the beam distribution before this peak stayed almost unchanged. This indicates that the signal background from the cables have a strong effect on the signal measured only when the beam core is hitting the cable, if the cables stays sufficiently far from the beam core ($>3\sigma$), such effects from the cables can be neglected.

8.4.2 Cut of beam halo by the apertures

Except for the "strange" peak observed on the beam halo distribution, an obvious edge of cut can also be found at ∼30 mm and ∼90 mm location of the beam halo distribution as shown in Fig. 8.11. We assume that this edge is caused by the cut of the beam halo by the apertures as simulated in section 4.4.

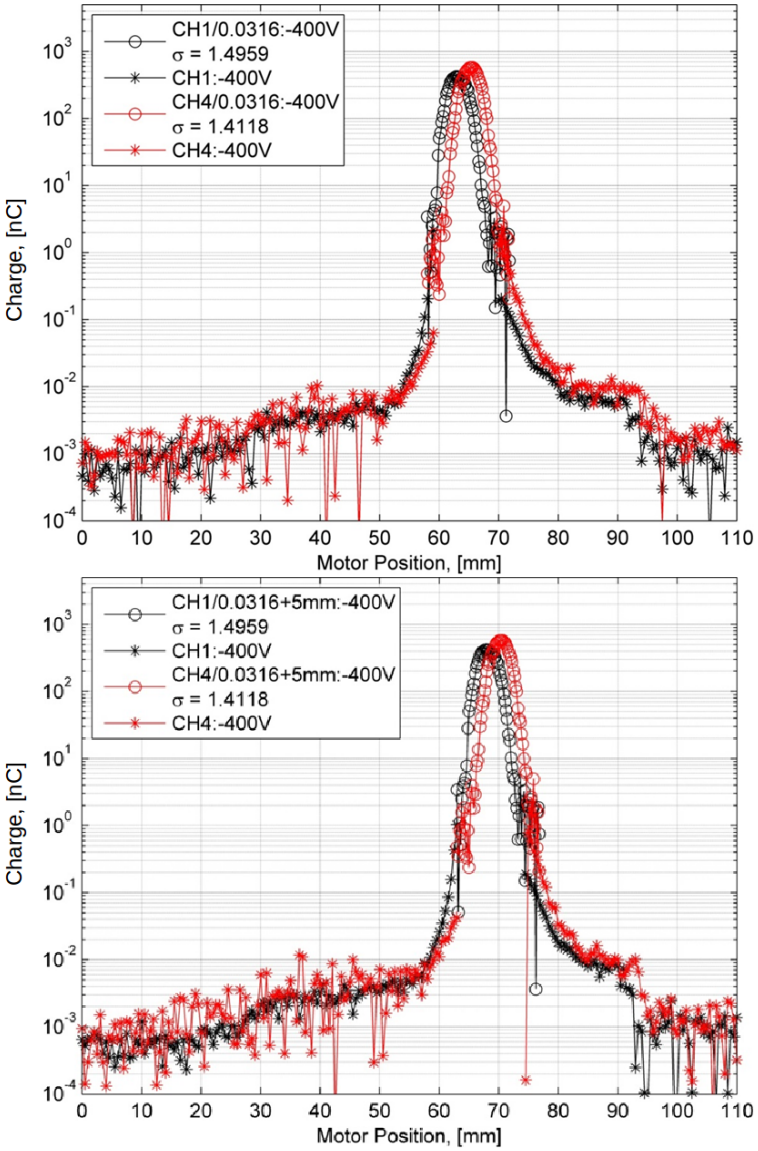

Figure 8.11: Beam halo distribution before (upper) and after (lower) moving the beam horizontally at the QF9AFF location by 3mm

In order to investigate which aperture has caused this cut, in the experiment, we moved the beam horizontally at the QF9AFF quadrupole position from 0 mm to -3 mm to check the effect of cuts by apertures downstream of QF9AFF. The QF9AFF quadrupole is located 64.12 m from the beginning of the EXT line. We found that the cut position stays at around 30 mm on the left side (LE side) and around 95 mm on the right side (HE side) (see Fig. 8.11). This confirms that the cut is given by the apertures downstream of QF9AFF. As mentioned in section 4.4, we would expect that this cut is given by the C-Band BPM installed after the SF5FF sextuple. However, the cut at this position is at around $20\sigma_x$ position (σ_x measured by CH1), which is much further than $16\sigma_x$ as we expected.

As the distance between two edges of cut is around 65 mm, we suspected that this cut is given by the beam pipe installed after the BDUMP, which has a diameter of 63 mm (see Fig.7.3). Therefore, we changed the BDUMP bending magnet strength to move the beam horizontally in the bending magnet.If the cut is due to upstream apertures, then the cut position should move together with the beam core, if not, then the cut will still stay at the same position. By changing the strength by +4 A the beam core is moved by around 5 mm toward the LE side. In Fig. 8.12 we show the result of change of the beam halo distribution with the change of BDUMP bending magnet strength. From the figures we can see that by changing the BDUMP bending magnet strength from the initial value of 367.75 A (+0 A) to 381.75 A (+14 A), 389.75 A (+22 A) and 395.75 A (+28 A), the cut position of beam halo stays always at around 95 mm. Thus we can conclude that this cut of beam halo is due to the beam pipe after the BDUMP exit instead of the aperture of the C-Band BPM.

The simulated value in section 4.4 predicted a cut by the vacuum beam pipe installed after the BDUMP at around $\pm 25.8\sigma_x$ position, and the measured cut is at around $\pm 20\sigma_x$ position. Taking into account the small mismatch factor between simulation and measurement and the fact that the CH1 is slightly larger than real beam size, the expected cut should be at $\sim \pm 24.4\sigma_x$ position, which is quite consistent with the predicted value.

8.4.3 Beam halo distribution dependence on beam intensity

The effect of beam intensity changes on beam halo distributions was studied by changing the total beam intensity. The total beam intensity can be controlled by changing the

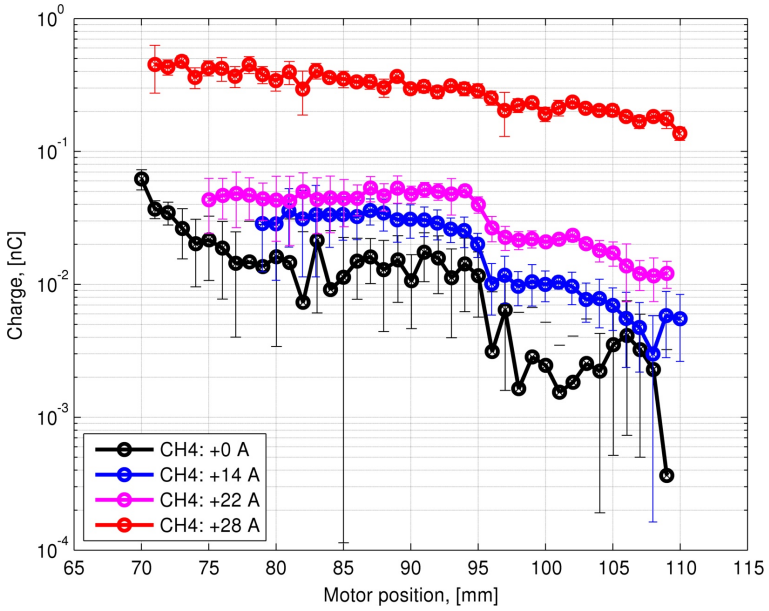

Figure 8.12: Beam halo distribution change on the HE side when the beam halo was moved toward the LE side by changing the BDUMP bending magnet strength.

intensity of the laser which is injected into the photon gun. In principle the laser intensity can be changed from 0% to 100% and the beam intensity can be changed from 0 to 10^{10}, however, as the ICT, which was used for the beam intensity measurement, is not sensitive to a beam intensity below 10^9 e^-, in this measurement we changed the beam intensity only from 1.1×10^9 to 2.5×10^9 and to 4.5×10^9 e^-. The measurement results are shown in Fig. 8.13. As the measurements were done before fixing the cable, the "strange peak" on the HE side can be observed. However, this doesn't affect the halo distribution before this peak.

An increase of beam halo population can be observed after increasing the beam intensity in Fig. 8.13 (a) and (b). Besides, from Fig. 8.13 (c) and (d), it can be seen that after normalising the beam intensity to 10^9 for all the data, the shapes of the beam halo distributions are quite consistent for different intensities. Thus, we can conclude that for the intensity change that we have applied, almost no change on the horizontal beam halo distribution was observed. As the beam intensity dependence is mainly expected on the vertical plane (since $\sigma_y \ll \sigma_x$), we expect to see the beam halo distribution change in the vertical plane rather than in the horizontal plane as predicted by the simulation done in Reference [73].

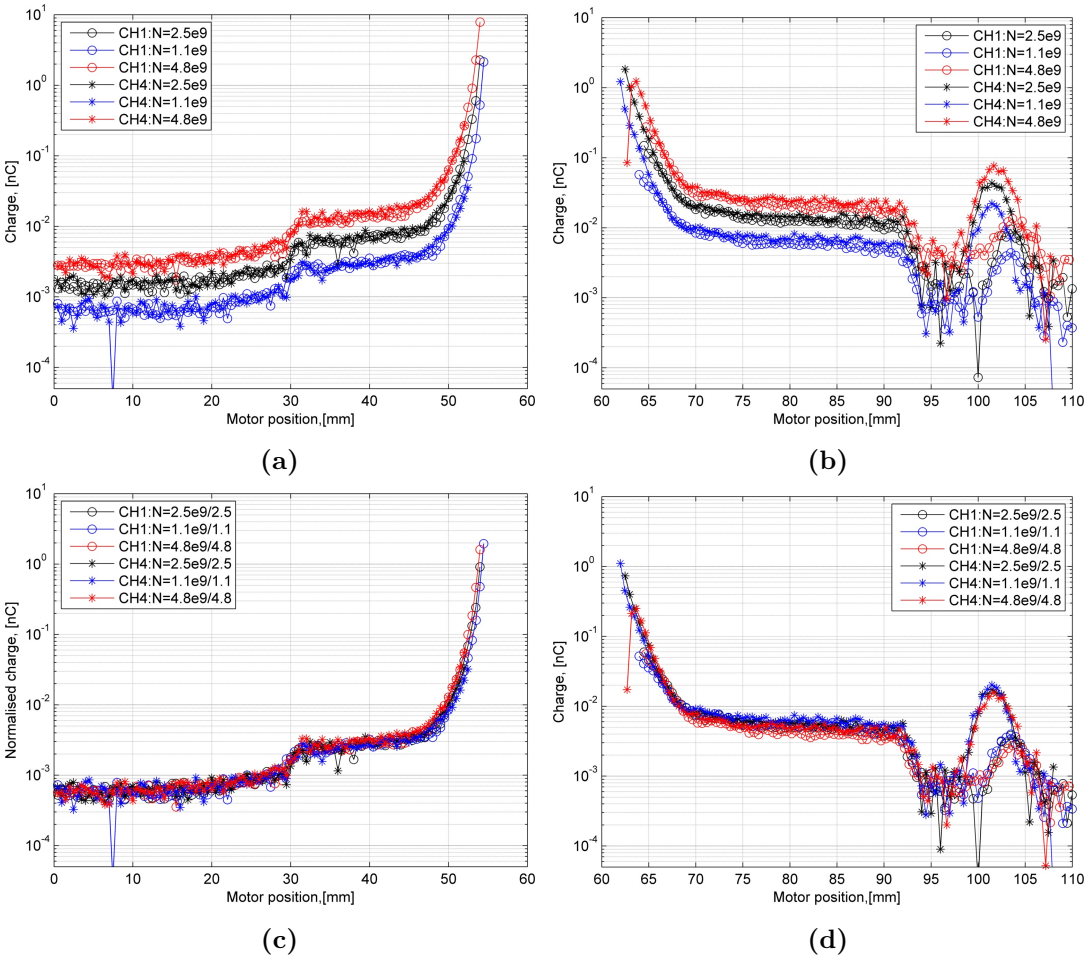

Figure 8.13: Horizontal beam halo distribution measured for different beam intensity before (top) and after (bottom) normalization

8.4.4 Beam halo distribution dependence on beam optics

The dependence of the beam halo distribution on the beam optics is quite important. Measurements of the effect of the beam optics on the horizontal beam halo distribution were performed during the Nov.-Dec. Run in 2014. During the run, three optics were used for different studies: BX10BY0.5 (ultra low β_y), BX10BY1 (nominal β_y) and BX100BY1000 (large $\beta_{x,y}$). The β_x and β_y values for different optics are shown in Table.8.3. From the table it can be seen that while there is no difference in β_x value between the BX10BY0.5 and the BX10BY1 optics, in the BX100BY1000 optics the β_x is much smaller than the other two optics. Therefore, we expect to see a decrease of

beam halo in the BX100BY1000 optics.

	BX10BY0.5		BX10BY1		BX100BY1000	
	β_x (m)	β_y (m)	β_x (m)	β_y (m)	β_x (m)	β_y (m)
IP	4.011e-02	5.600e-05	4.000e-02	1.000e-04	4.000e-01	1.000e-01
post-IPW	9.777e+00	6.995e+03	9.806e+00	3.906e+03	1.377e+00	4.006e+00
DS	4.355e+02	2.671e+05	4.367e+02	1.492e+05	4.407e+01	1.492e+02

Table 8.3: β_x^* and β_y^* values for different optics

Fig. 8.14 shows the measured horizontal beam halo distribution on the LE side (left) and HE side (right). Data binning was applied to reduce the fluctuation.

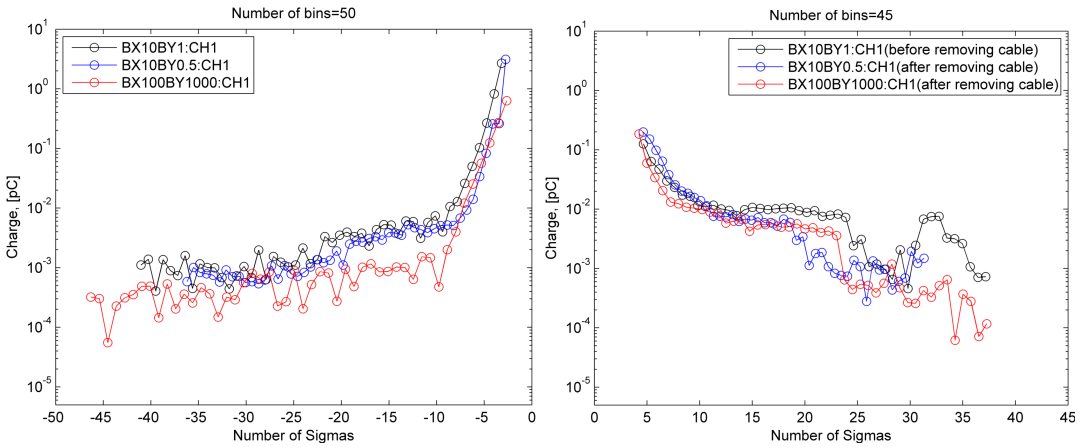

Figure 8.14: Beam halo distribution measured using CH1 for different optics

On the LE side, it can be seen that the distribution for BX10BY1 and BX10BY0.5 is quite consistent and for BX100BY1000 we observe less beam halo as expected especially in the region from -10σ to -20σ. The region with <-20σ the signal is dominated by the pick-up signal. For the investigation of the possibility to detect the Compton recoil electrons on the LE side, we will only use the distribution measured on the LE side for further analysis in Chapter 9.

On the HE side, data for BX10BY1 was collected before removing the cables, therefore it has a higher beam halo level than BX10BY0.5 in the region >20σ. However, the signal level for BX100BY1000 is not much less than the other two optics as on the LE side.

Comparing the signal level on the LE side with the HE side, larger signal level on the HE side was observed. Similar asymmetrical distribution was observed in the measurements using wire scanners. The results are compared to the wire scanner measured results in the next section.

8.5 Comparison of horizontal beam halo distributions

After the BDUMP bending magnet, at the DS location the horizontal beam size is dominated by dispersion:

$$\sigma^2 = \sigma_\beta^2 + \sigma_p^2 = \epsilon_x \beta_x + (D_x \frac{\Delta E}{E})^2 \tag{8.3}$$

where the dispersion D_x=1.294 m and the energy spread $\frac{\Delta E}{E}$=8×10^{-4}, β_x =436.74 m and ϵ_x=2 nm as shown in Table 8.4. The calculated $\sigma_\beta = 934.6$ μm and the $\sigma_p = 1035.2$ μm, therefore, the expected beam size at DS location is 1.39 mm. The measured beam size by CH2 is 1.35 ± 0.03 mm (see Table 8.2).

	BX10BY0.5	
	β_x (m)	D_x (m)
MW2X	3.918	0
post-IPW	9.777	0.0874
DSv	436.74	1.294

Table 8.4: Beta function and dispersion function values at different locations for BX10BY0.5 optics

Since the dispersions are almost 0 and 0.0874m at MW2X and post-IPW positions, respectively, which are both small comparing with the beta function, the contribution of dispersion on the beam size and also on the horizontal beam halo distribution is negligible. Therefore, the fitted beam halo distribution with the parametrizations done in 2005 and 2013 can be considered as a fit for σ_β and it can not be compared to the beam halo distribution measured at the DS location directly.

However, as shown in Eq. 8.3, if we exclude the contribution from the dispersion function to the beam distribution and plot the measured beam distribution as a function of σ_β, then it might be comparable with the WS measured distribution.

By excluding the σ_p = 1035.2 μm from the measured beam size of 1.3496 mm by CH2, we can obtain the σ_β as:

$$\sigma_\beta = \sqrt{\sigma^2 - \sigma_p^2} = 0.866mm \tag{8.4}$$

Using this calculated σ_β, we compared the measured beam halo distribution with the 2005 parametrisation.

Fig. 8.15 shows the comparison of DSv measured beam halo with the the 2005 model with and without the contribution from dispersion. Since 30 dB attenuator was added for the beam core measurement, the singal in the beam core is divided by a factor of 0.0316. The curve from 2005 model is normalised to the strength of DS signal using the "fitting model normalization method" described in Section 5.3.1. The X axis in the upper plot is number of σ, where σ=1.3496 mm. And the lower plot is in number of σ_β, where σ_β=0.866 mm. The enlarged beam halo distribution measured by CH2 and CH3 is shown in Fig. 8.16. For CH3, the calculated σ_β=0.804 mm.

It can be seen that by excluding the contribution from dispersion, the beam halo distribution fits quite well on the HE side (right side on the plot), while on the LE side (left side on the plot) it is a little bit less than the 2005 model. This result is consistent with the post-IPW measured results as shown in Fig.8.17. It worth to mention here that the HE side and LE side halo is inverted after the BDUMP bending magnet as shown in Fig.8.18.

In Chapter 5 we have mentioned that the post-IPW measured distribution fits well with the 2005 model as shown in Fig.8.17. From the 2005 measured result in the old ATF EXT line, we can also see an asymmetry distribution between LE side and HE side, which is consistent with the post-IPW result measured in 2013. The reason for this asymmetrical distribution is unknown. The old ATF EXT line and ATF2 beam line is shown in Fig.8.18.

From the comparison of measurements done using the DSv and the wire scanners in the old ATF EXT line and in the new ATF2 EXT line, we can conclude that the beam halo horizontal distribution as a function of number of σ_β is consistent. This may indicate that beam halo at ATF2 is dominated by the betatron halo instead of energy halo, which seems not to be observable in the present measurements. However, further measurements in high dispersion region are required to study the energy halo. Besides, the investigation of the reason for the asymmetrical horizontal beam distribution (more

halo on the HE side than on the LE side) is also important for the understanding of beam halo formation in the damping ring.

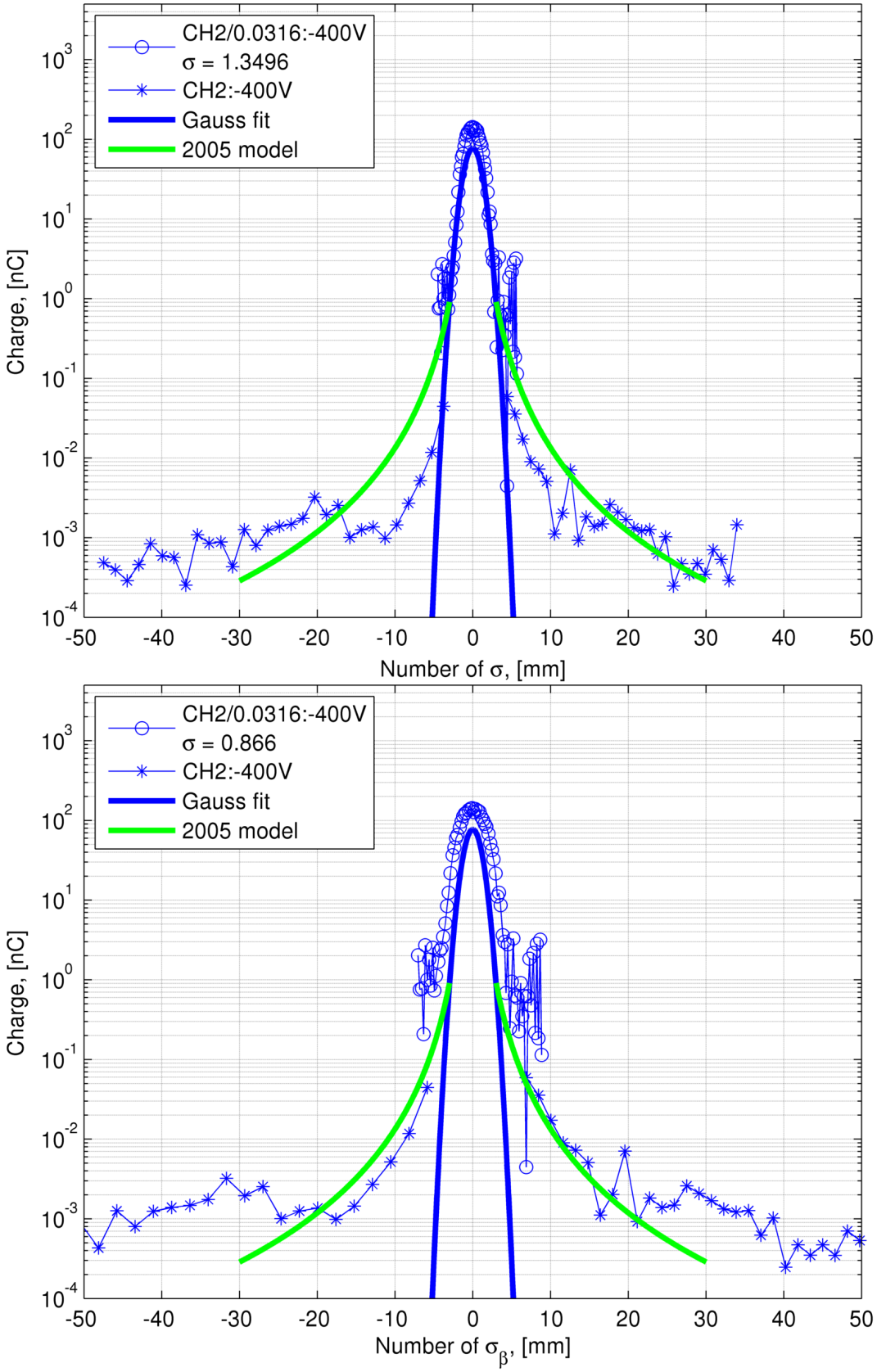

Figure 8.15: Horizontal beam and beam halo distribution measured using DS CH2 with (upper) and without (lower) contribution from dispersion (data taken on 18-12-2014)

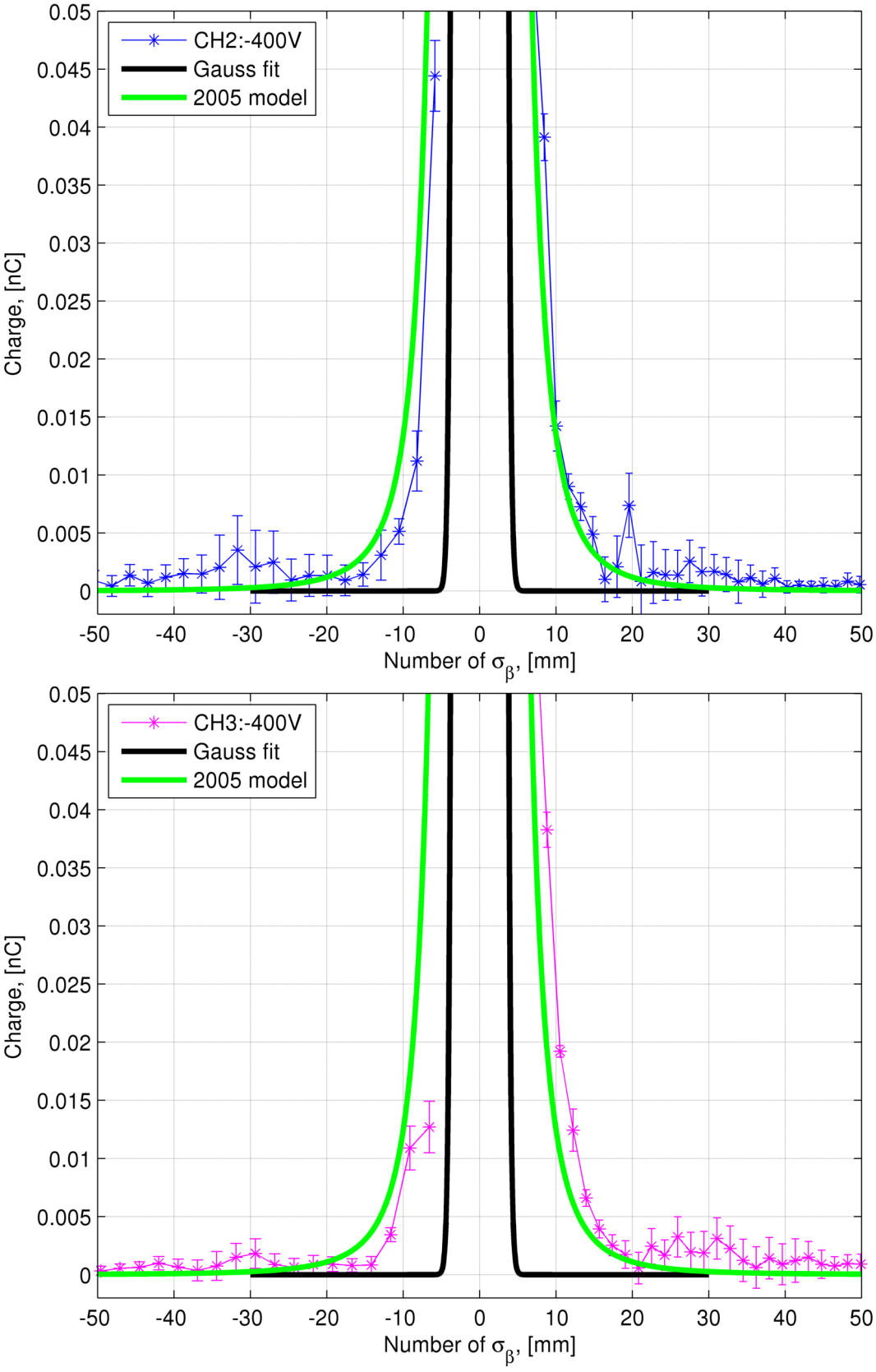

Figure 8.16: Enlarged horizontal beam halo distributions measured using DS CH2 (upper) and CH3 (lower) without contribution from dispersion (data taken on 18-12-2014).

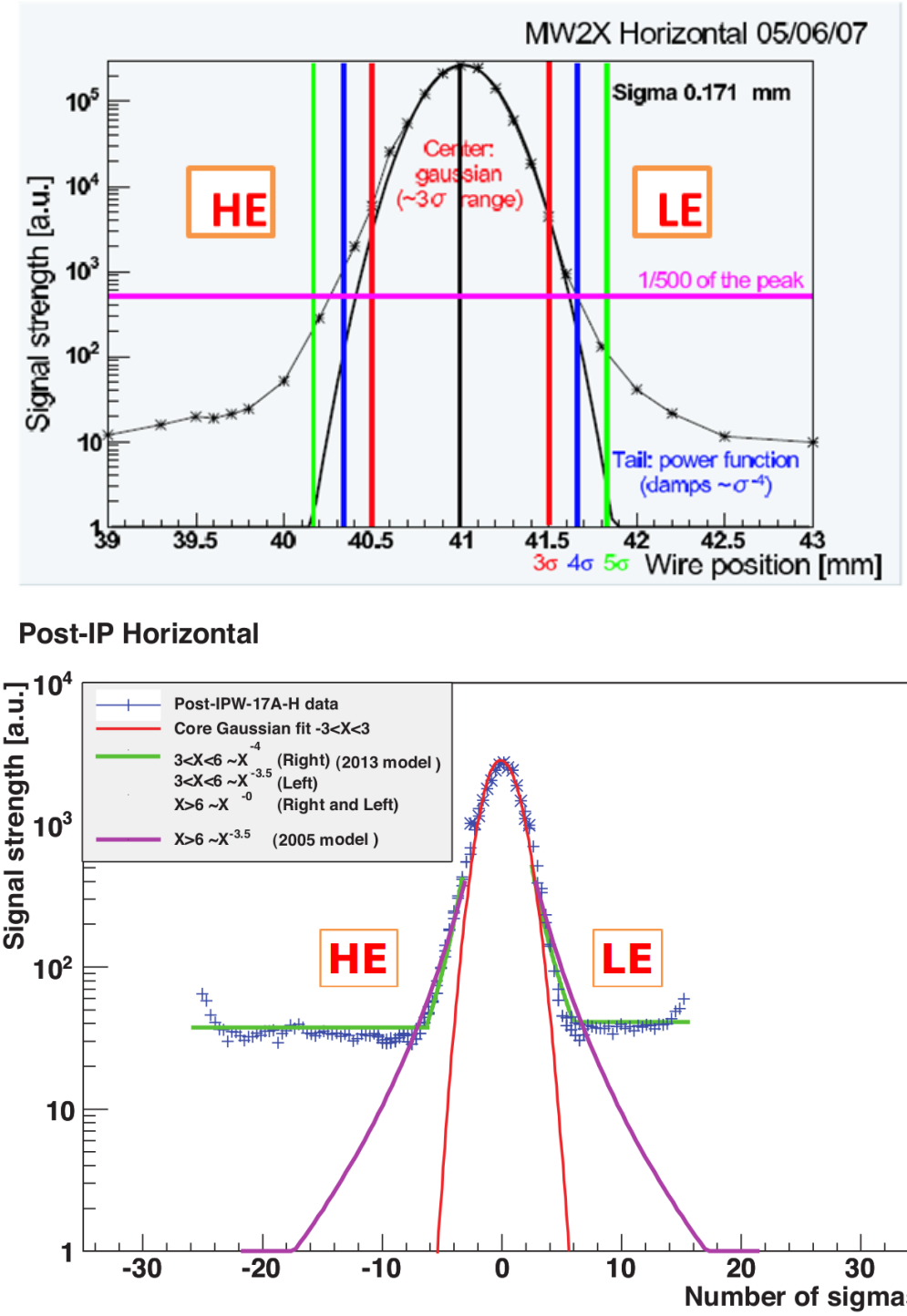

Figure 8.17: Horizontal beam distributions measured by MW2X in 2005 (upper) and by post-IPW in 2013 (lower)

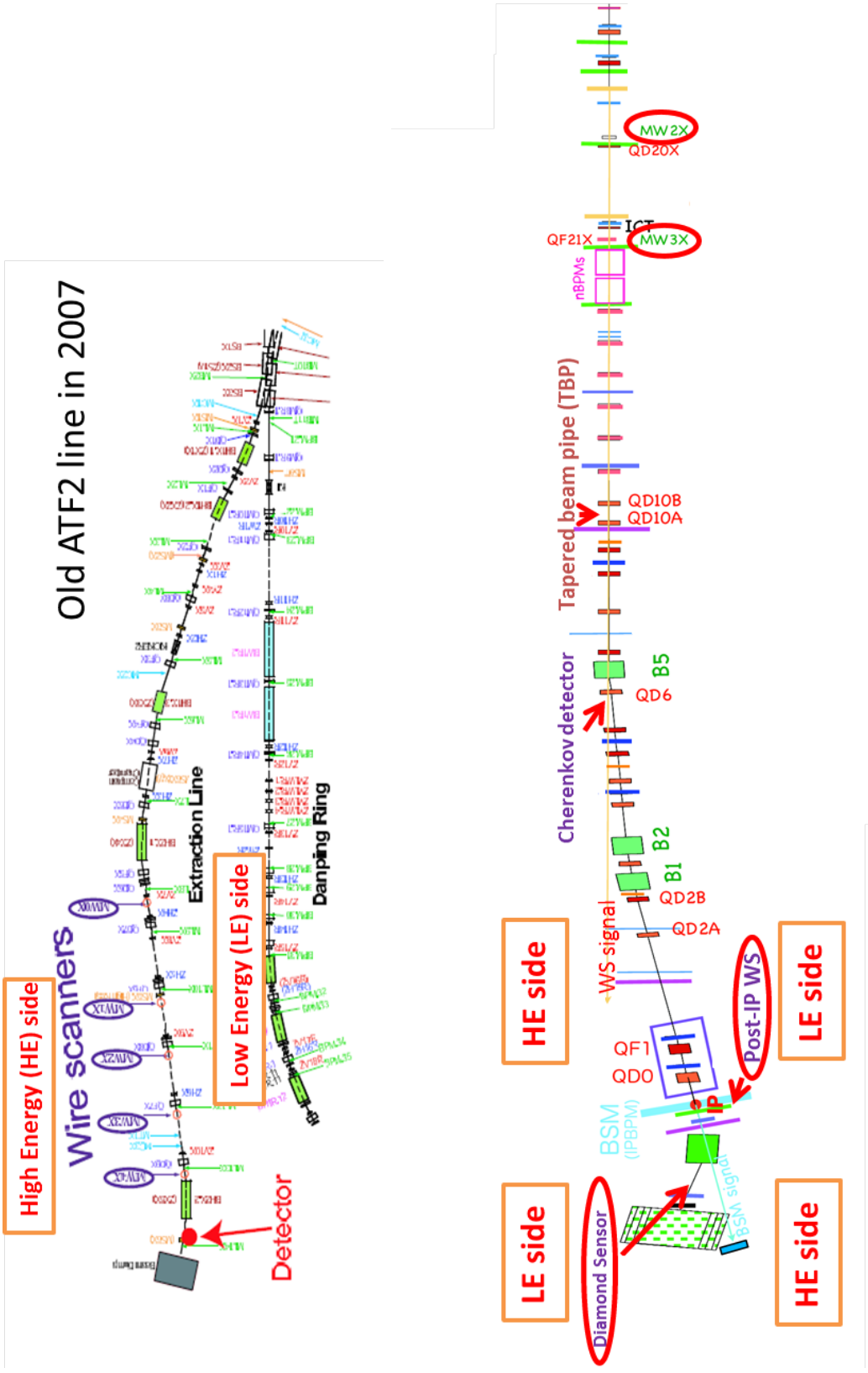

Figure 8.18: Old ATF EXT line (upper) and ATF2 beam line (lower)

8. BEAM HALO HORIZONTAL DISTRIBUTION MEASUREMENTS AT ATF2